

Non-newtonian Fluids



by

Adarsh Prajapati

Report submitted for

Supervised Learning Project

PROF. ABHIJEET KUMAR

DEPARTMENT OF MECHANICAL ENGINEERING
INDIAN INSTITUTE OF TECHNOLOGY BOMBAY

May 2024

Abstract

This project aims to conduct a comprehensive literature review on the behavior of non-Newtonian fluids across various scientific disciplines. Non-Newtonian fluids exhibit complex rheological properties, deviating from the linear relationship between stress and strain rate observed in Newtonian fluids. Understanding their behavior is crucial for applications in industries such as food processing, pharmaceuticals, cosmetics, and petroleum engineering.

The study will encompass a wide range of literature sources, including research articles, conference papers, and academic texts, to provide a holistic perspective on the subject. Key areas of focus will include the classification of non-Newtonian fluids, their flow characteristics, and the underlying mechanisms governing their behavior. Special attention will be given to the differences in behavior exhibited by various types of non-Newtonian fluids, such as shear-thinning, shear-thickening, their primary and secondary breakup, the drop impacts, and air blast atomization.

Through this comparative analysis, the project aims to elucidate common trends, challenges, and advancements in the understanding of non-Newtonian fluid behavior. Moreover, it seeks to identify gaps in current knowledge and propose avenues for future research. The findings of this study will not only contribute to the theoretical understanding of non-Newtonian fluids but also have practical implications for the design and optimization of processes involving these complex fluids in the future. One such application is being used as a liquid armor.

Table of Contents

1	Introduction	1
1.1	What is a Non-Newtonian Fluid?	1
1.2	Types of Non-Newtonian Fluids	2
1.3	Applications	3
1.4	Studying microstructures and fluids	4
1.4.1	Transmission Electron Microscope (TEM)	4
1.4.2	Scanning Electron Microscope (SEM)	4
1.4.3	Rheometer	4
1.4.4	Automatic Laser Granularity Analyzer	5
2	Analysis of various behaviours	6
2.1	Shear thickening Primary breakup	6
2.2	Shear thinning Primary breakup	10
2.3	Secondary Breakup with Airblast atomization	14
2.3.1	Shear thickening droplet	15
2.3.2	Shear thinning droplet	19
2.4	Drop Impact	22
2.5	Shear and Extensional Flow	25
3	Conclusion	30
3.1	Further Applications	30
3.1.1	Liquid Armor	30
4	References	34

Glossary

CABER Capillary Breakup Extensional Rheometer.

CST Continuous Shear Thickening.

DST Discontinuous Shear Thickening.

FSR Filament Stretching Extensional Rheometer.

Chapter 1

Introduction

1.1 What is a Non-Newtonian Fluid?

A non-Newtonian fluid is a fluid that does not follow Newton's law of viscosity, i.e, it has variable viscosity dependent on stress. In particular, the viscosity of non-Newtonian fluids can change when subjected to force. Most commonly, the viscosity (the gradual deformation by shear or tensile stresses) of non-Newtonian fluids is dependent on shear rate or shear rate history. In Newtonian fluids, the correlation between shear stress and shear rate is linear, and passes through the origin, with viscosity acting as the constant of proportionality. However, in non-Newtonian fluids, this relationship varies with the strain rate. Such fluids may even display viscosity that changes over time, making it impossible to establish a fixed viscosity coefficient.

The newton's law of viscosity is :

$$\tau_{xy} = \mu \frac{dv_x}{dy} \quad (1.1)$$

However, the non Newtonian fluids follow a power law :

$$\tau_{xy} = -m|\dot{\gamma}|^{n-1} \frac{dv_x}{dy} \quad (1.2)$$

where

- $|\dot{\gamma}|^{n-1}$ is the absolute value of the strain rate to the (n - 1) power
- $\frac{dv_x}{dy}$ is the velocity gradient
- n is the power law index

1.2 Types of Non-Newtonian Fluids

Non-newtonian fluids can be broadly categorised into 3 classes :

- Viscoelastic fluids
- Time-dependent viscosity
- Dilatant
- Pseudoplastic

Viscoelastic fluids: Viscoelastic fluids are a type of non-Newtonian fluid formed by a viscous component and an elastic one. For short, viscoelastic fluids are the blend of a solvent and some polymer. Examples of these are paints, DNA suspensions, some biological fluids and others from the chemical industry.[1]

Time dependent viscosity: Fluids classified as time-dependent fluids have viscosities that vary with the passing time. They are a kind of non-Newtonian fluid with structural changes that happen too slowly for equilibrium configurations to be maintained throughout deformation. Thixotropic fluids and rheopectic fluids are the two primary divisions of time-dependent fluids.

Dilatant: A dilatant is a non-Newtonian fluid where the shear viscosity increases with applied shear stress. This can readily be seen with a mixture of cornstarch and water (sometimes called oobleck), which acts in counterintuitive ways when struck or thrown against a surface.

Pseudoplastic: A non-Newtonian fluid known as a pseudoplastic fluid exhibits shear thinning behaviour, meaning that its viscosity lowers as the shear rate rises. It is often observed in polymer solutions and molten polymers, as well as complex fluids and suspensions like ketchup, whipped cream, blood, paint, and nail polish.

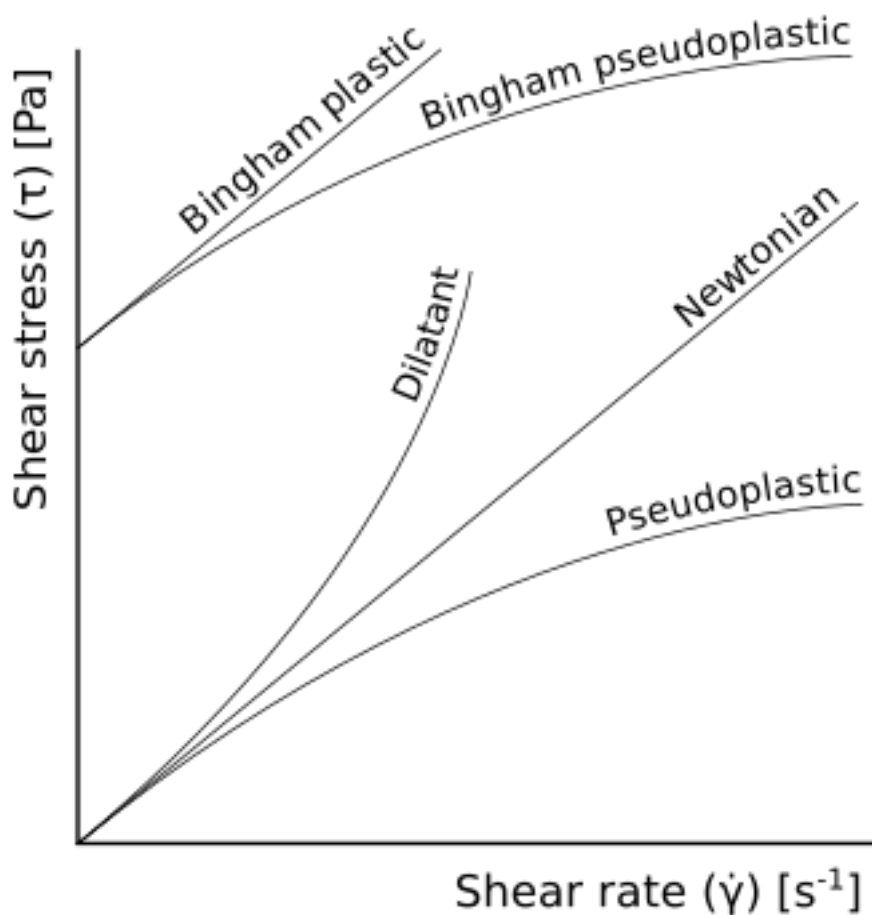


Figure 1.1: Classification of fluids with shear stress as a function of shear rate: Pseudoplastic, Bingham plastic and Bingham pseudoplastic all show reduction in apparent viscosity with increasing shear rate

1.3 Applications

Different types of non-Newtonian fluids find applications across various industries. Shear-thinning fluids like polymer solutions are used in food processing (sauces, dressings), cosmetics (lotions, creams), and pharmaceuticals (ointments, suspensions). Shear-thickening fluids, such as cornstarch suspensions, are utilized in body armor for impact resistance and damping systems. Viscoelastic fluids like polymer melts are essential in polymer processing for molding and extrusion. Yield-stress fluids like toothpaste and drilling muds are employed in personal care products and oil drilling, respectively. Understanding their behavior is crucial for optimizing processes and designing products in these diverse fields.

1.4 Studying microstructures and fluids

1.4.1 Transmission Electron Microscope (TEM)

TEM allows you to observe details as small as individual atoms, giving unprecedented levels of structural information at the highest possible resolution. As it goes through objects it can also give you information about internal structures, which SEM cannot provide. TEM is, however, limited to samples that can be thin enough to let electrons pass through them. This thinning process is technically challenging and requires additional tools to perform.

1.4.2 Scanning Electron Microscope (SEM)

SEM functions similarly, sweeping the electron beam across the sample and recording the electrons that bounce back. This technique allows you to see the surface of just about any sample, from industrial metals to geological samples to biological specimens like spores, insects, and cells. While SEM cannot see features to the same level of detail as TEM, it is much faster, less restrictive, and can sometimes be performed with limited or no sample preparation.

1.4.3 Rheometer

A rheometer is a laboratory device used to measure the way in which a viscous fluid (a liquid, suspension or slurry) flows in response to applied forces. It measures the rheology of the fluid (viscosity, shear rate, shear stress, normal force, etc.). There are two distinctively different types of rheometers. Rheometers that control the applied shear stress or shear strain are called rotational or shear rheometers, whereas rheometers that apply extensional stress or extensional strain are extensional rheometers. Most commonly used Extensional rheometers are CaBER(capillary breakup rheometer), and FiSER(filament stretching extensional rheometer). Most rheometers use the same measurement geometry (cone, plate, parallel plate, concentric cylinder, etc.).

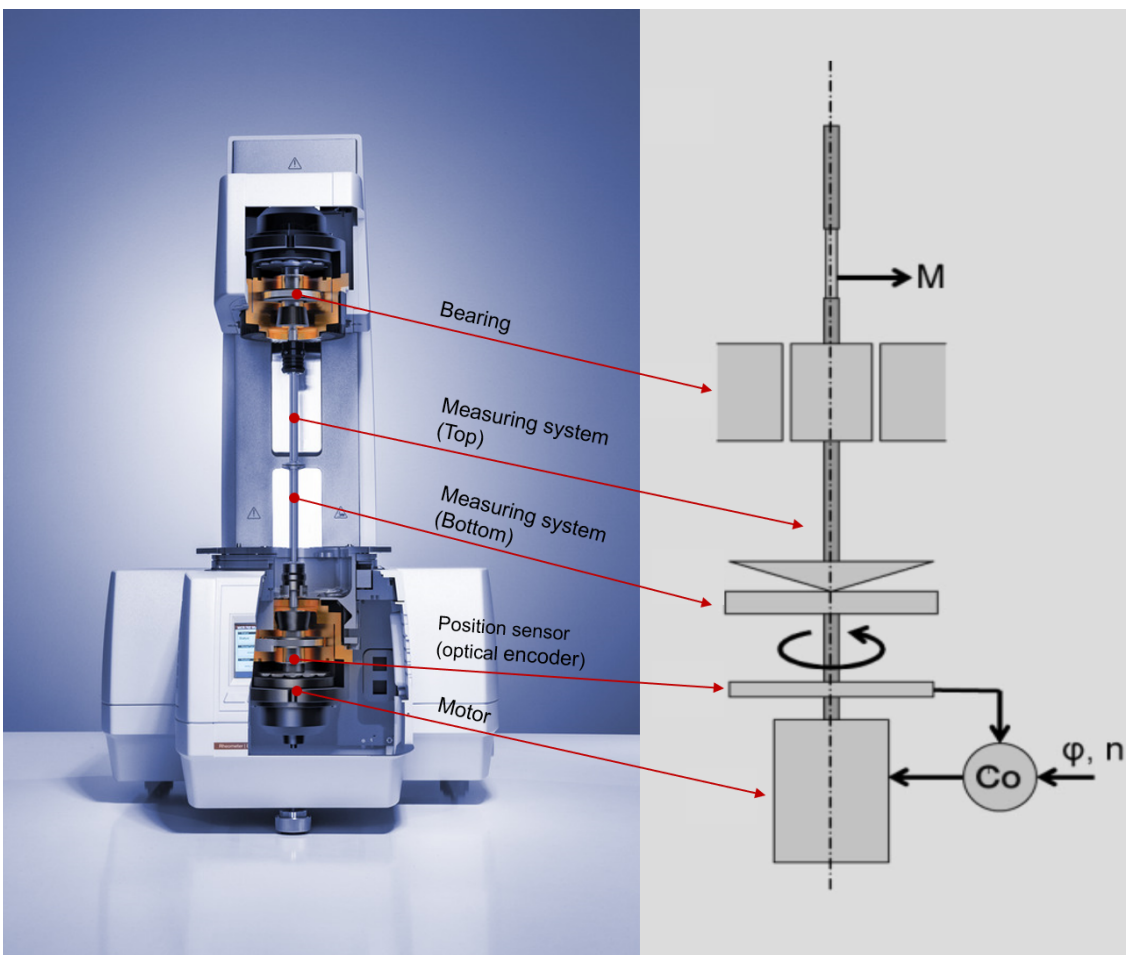


Figure 1.2: Strain-controlled (CR-)rheometer: A speed ω or a deflection angle ϕ is applied and the resulting torque M is measured by an additional torque re-balance transducer.

1.4.4 Automatic Laser Granularity Analyzer

A laser particle analyzer, also known as a laser diffraction particle size analyzer, uses a laser beam to measure the size of particles in a material by measuring the angle of light scattered by the particles as they pass through the beam. They can be used for both wet samples and dry powders, and can determine the particle size distribution over a wide dynamic measurement range.

Chapter 2

Analysis of various behaviours

Contents

2.1	Shear thickening Primary breakup	6
2.2	Shear thinning Primary breakup	10
2.3	Secondary Breakup with Airblast atomization	14
2.3.1	Shear thickening droplet	15
2.3.2	Shear thinning droplet	19
2.4	Drop Impact	22
2.5	Shear and Extensional Flow	25

2.1 Shear thickening Primary breakup

The analysis of breakup morphology in cornstarch-water suspensions with varying rheological behaviors reveals a distinct progression through three stages: thinning, thickening, and dilution. An important parameter to watch out for here is the droplet threat diameter D_m and its relation with the time left for droplet breakup, where it would eventually become 0.

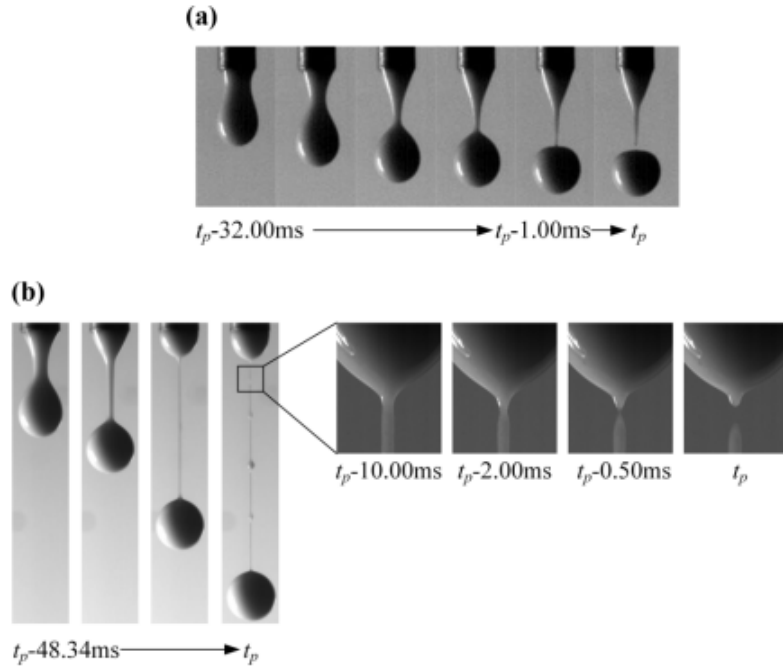


Figure 2.1: The breakup and throat morphology near the breakup of a droplet of suspension at volume fractions of (a) $\phi = 35\%$ and (b) $\phi = 41\%$, where t_p is the time of breakup

$$D_m \propto (t_p - t)^\beta$$

$$\eta(\dot{\gamma}) = K\dot{\gamma}^{n-1}$$

TABLE II. Characteristic indexes of suspension breakup β and fluid behavior n for different breakup modes.

Modes of breakup	n	β
Thinning stage	<1	2/3
Thickening stage	1–3	1/5
Diluted stage	>3	1

The experimental results indicated that the formation and breakup processes of cornstarch-water suspension droplets of different volume fractions ($35\% < \phi < 51\%$) were greatly influenced by their rheological properties. A suspension droplet entered the thinning stage when it exhibited shear thinning behavior or its apparent viscosity was constant. The throat diameter reduces rapidly and symmetrically. The suspension droplet enters the thickening stage when CST was exhibited because the frictional force between the particles in suspension was enhanced. The suspension throat shrank much more slowly, and

the throat diameter followed a power law, $D_m \propto (t_p - t)^{\frac{1}{5}}$. The suspension droplet entered the diluted stage when it exhibited DST. The diluted suspension formed at the throat due to the self-diluted effect and finally pinched off.

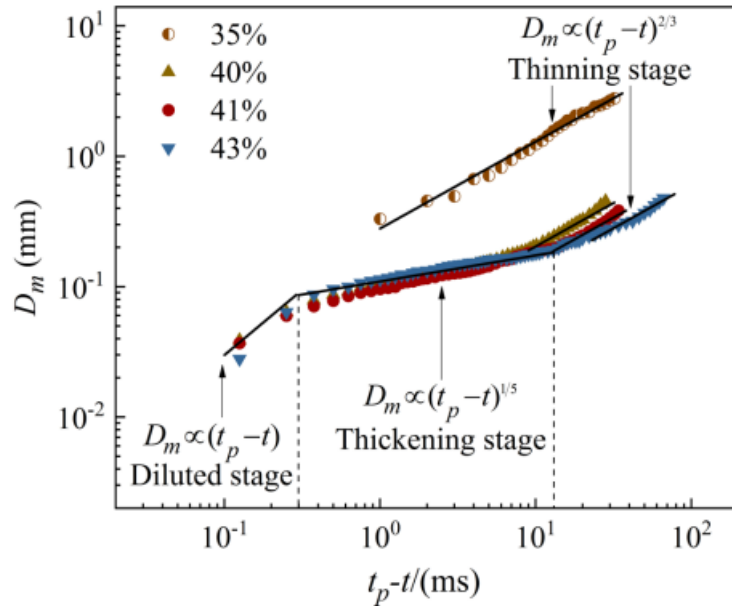


Figure 2.2: Development of the throat diameter D_m for $\phi = 35\%-43\%$, where t_p is the time of breakup.

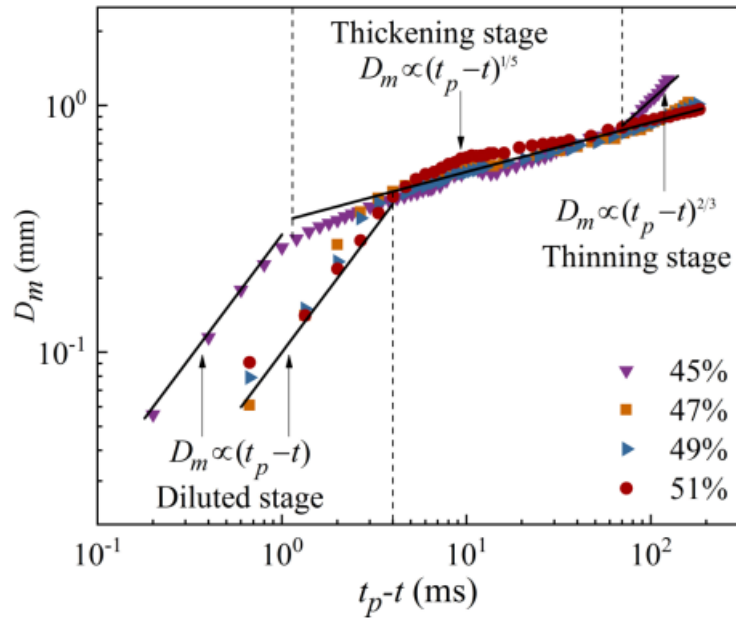
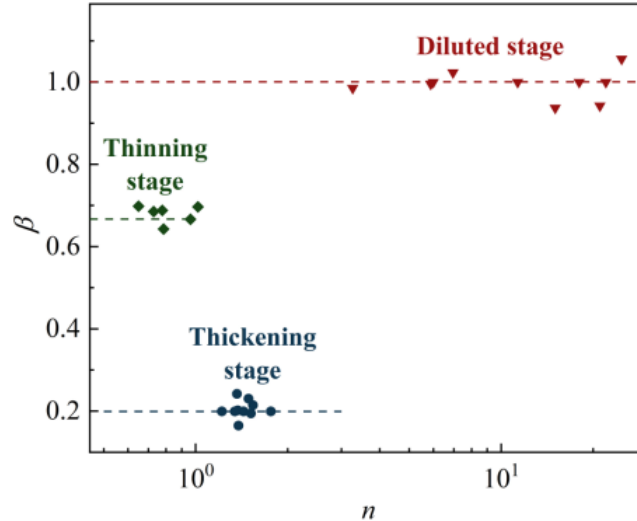


Figure 2.3: The development of the throat diameter D_m for $\phi = 45\%-51\%$, where t_p is the time of breakup



. The phase diagram of suspension breakup for different rheological properties.

When the shear rate reaches the critical shear stress, the apparent viscosity of these suspensions abruptly surges. The amplitude of the apparent viscosity increases by up to two orders of magnitude, which researchers refer to as DST.

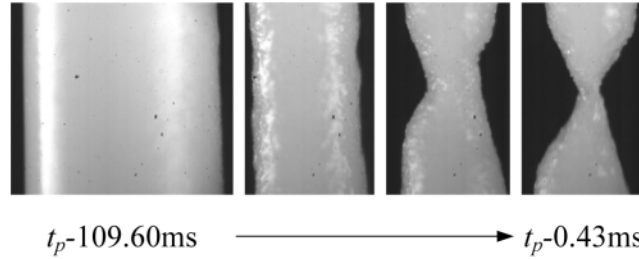


FIG. 11. Development of surface roughness during the breakup process.

An intriguing phenomenon emerges when the volume fraction of the suspension exceeds 43%, leading to the formation of a slip plane. This phenomenon bears resemblance to a solid-like behavior, akin to a cylindrical metal rod undergoing uniaxial tensile loading.

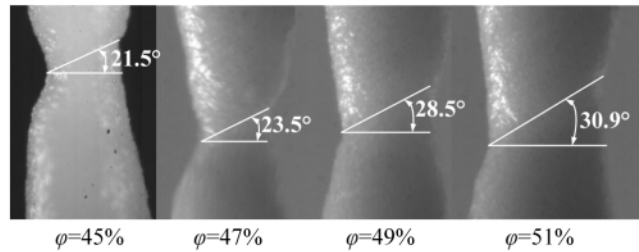


FIG. 8. The angle of the slip plane of the suspension at various volume fractions prior to breakup.

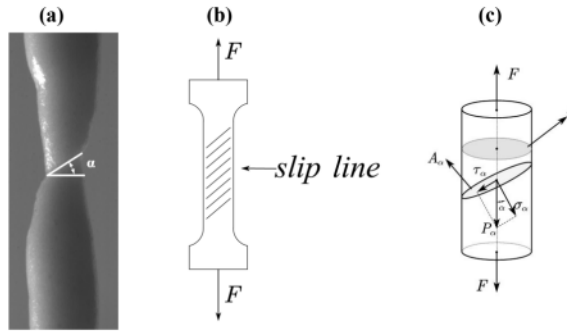
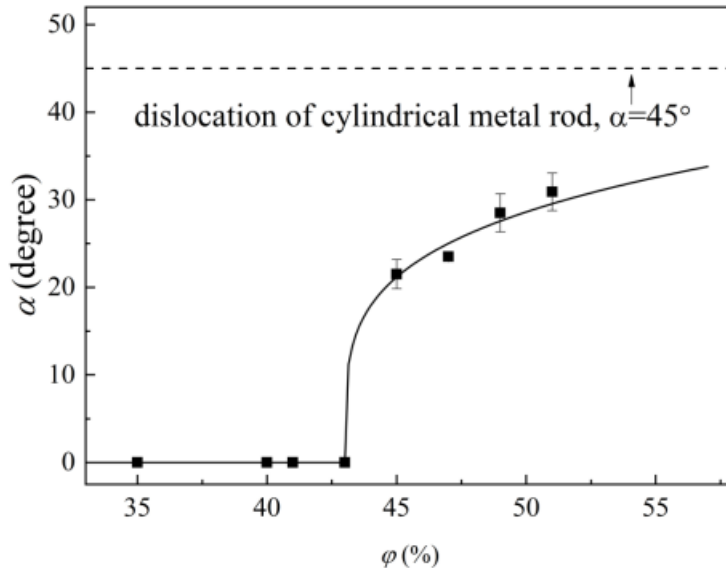


FIG. 12. (a) The throat morphology near the breakup of a cornstarch-water suspension droplet. (b) Slip lines in the area of plastic deformation in a metal rod consisting of single crystals. (c) Force analysis of a cylindrical metal rod under a uniaxial tensile force.

The Tresca criterion states that fracture always occurs along the maximum shear stress plane, i.e., at $\alpha = 45$.



2.2 Shear thinning Primary breakup

The study examines the formation of Newtonian and non-Newtonian shear-thinning drops in air, focusing on geometrical parameters such as drop elongation length, minimum neck diameter, and current contact angle. Various fluids including water, glycerin solutions (79%, 89%, and 94% w/w), and Carboxymethyl cellulose (CMC) solutions (ranging from 0.5% to 1.5% w/w) are investigated.

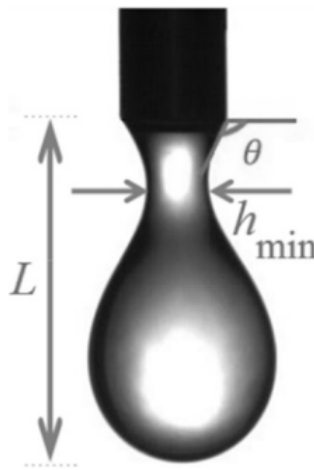


Figure 2.4: Drop length (L), neck thickness (h_{min}) and contact angle between the drop and the needle tip (θ).

Two primary regimes of drop formation are identified: dripping and jetting. In the dripping regime, low injection flow rates result in separate droplets exiting the nozzle tip due to dominant surface tension forces. With increased flow rates, the liquid transitions into a continuous jet that eventually breaks up into smaller drops downstream due to Rayleigh instabilities. The following results are for the dripping region only.

The detached drop size exhibits a continuous increase with increasing flow rate. However, upon reaching a critical flow rate, the drop size diminishes and deforms into an irregular shape.

Drop breakup length

Furthermore, drop size augmentation correlates with increases in nozzle radius and surface tension. By reducing the fluid viscosity, the viscous stresses decrease and therefore, in order to keep the difference in the surface stresses constant, the pressure in the neck region increases. Consequently, the rate in which the fluid exits the neck region increases and the drop detachment occurs faster. As a result, the drop length decreases.

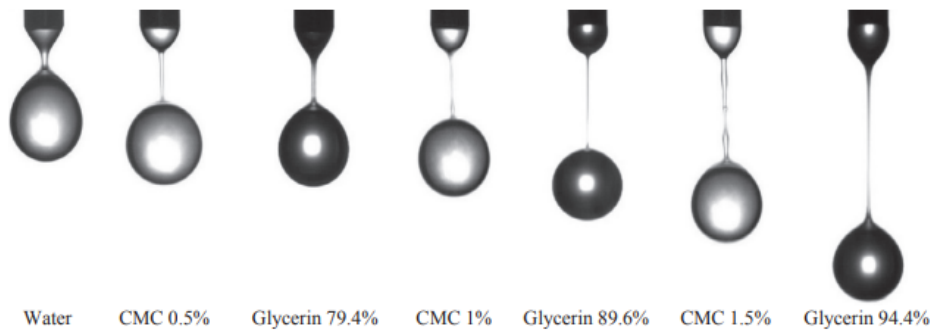


Fig. 8. Images of different drops 1 ms before the moment of detachment for flow rate of $Q = 150 \text{ mL/h}$ and needle outer diameter of $D_0 = 2.2 \text{ mm}$.

As the drop neck narrows, its surface curvature decreases, leading to an increase in capillary pressure. Consequently, the liquid extrudes from the needle at a higher rate, resulting in rapid elongation of the liquid filament until the drop detaches from this narrow liquid strip.

Initially, before the appearance of the drop neck, differences between Newtonian and non-Newtonian drops are negligible. However, as the necking process initiates, the drop length undergoes exponential changes over time, revealing clear distinctions among various fluids.

Temporal relation

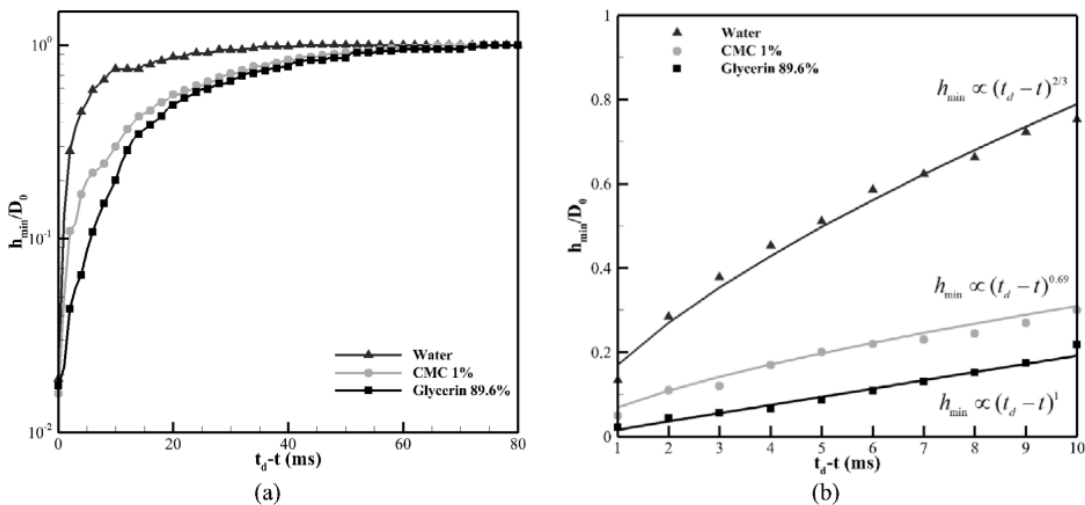


Figure 2.5: . (a) Non-dimensional ratio of the neck thickness to needle outer diameter as a function of the relative time, (b) fitted curves showing the non-dimensional ratio of the neck thickness to needle outer diameter as a function of the relative time at the last 10 ms of the drop formation process.

Contact angle

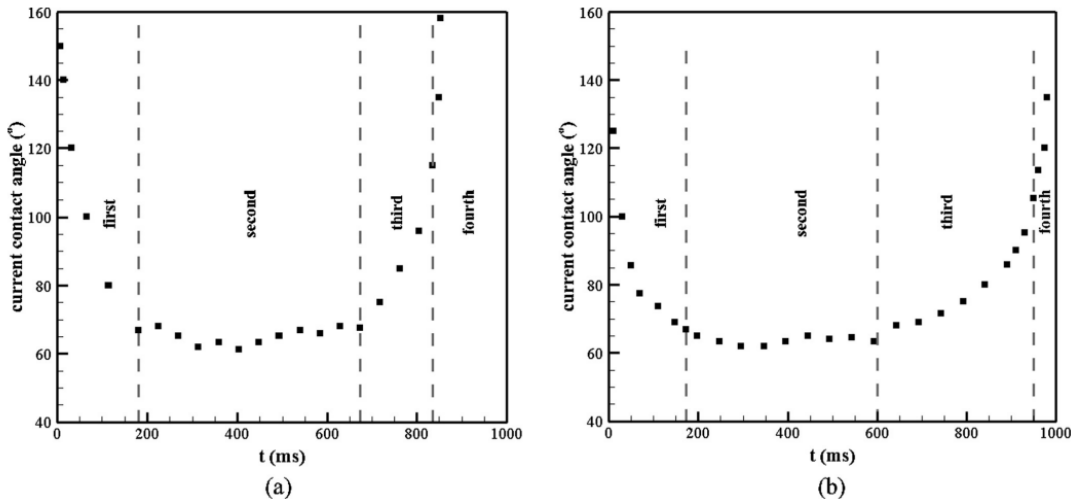


Figure 2.6: Instantaneous contact angle of (a) water and (b) CMC 1% drops as a function of the formation time

Drop formation frequency

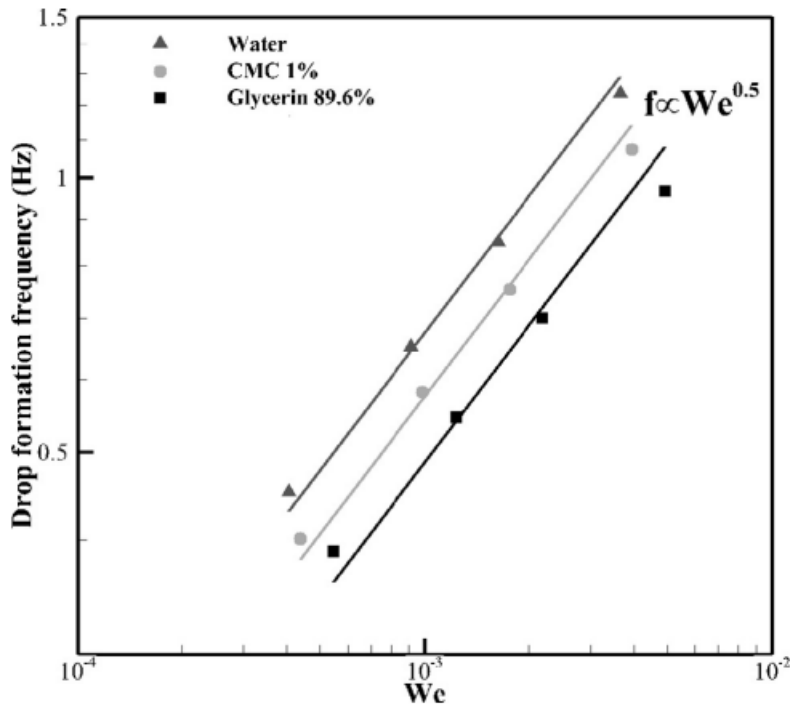


Figure 2.7: Drop formation frequency as a function of the Weber number

Satellite drop formation

In the dripping regime, a significant phenomenon is the deformation of the liquid filament connecting the drop to the fluid at the needle tip. After detachment, if surface

tension dominates inertial forces, the liquid filament merges with the fluid at the needle tip without breaking. However, if inertial forces prevail, high deformation and capillary pressure lead to filament detachment, forming satellite drops. The length of the liquid filament correlates with the likelihood of satellite drop formation. While water filaments lack sufficient elongation for satellite drop formation, high-viscosity liquids like CMC 1% and CMC 1.5% exhibit satellite drops due to pronounced elongation. Surface tension forces propel the satellite drop upwards, where it merges with the hanging drop. Increased satellite drop volume enhances gravitational force, limiting upward movement or causing downward motion if volume exceeds a critical threshold.

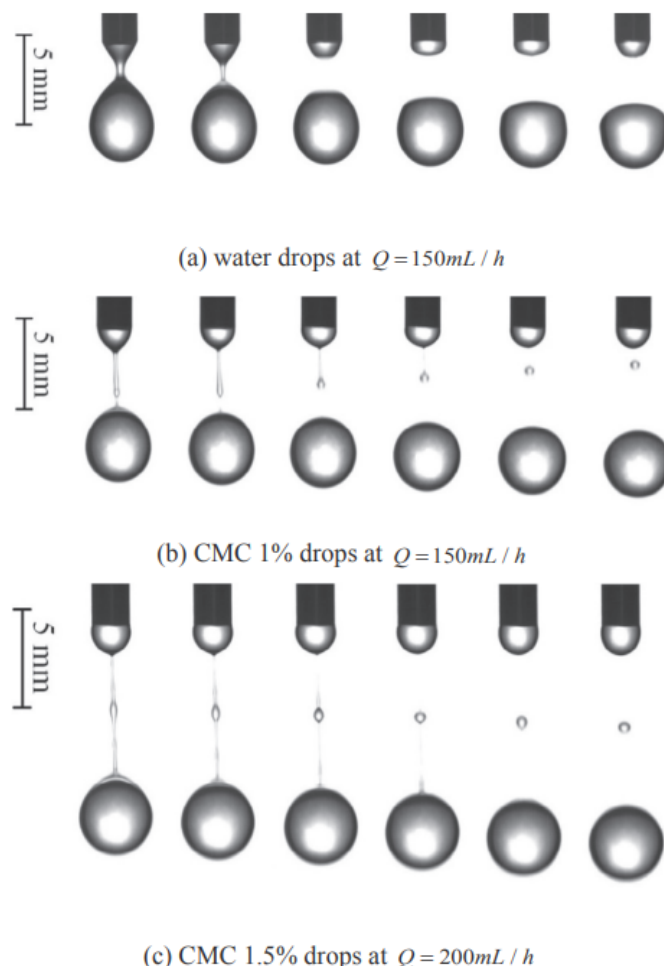


Fig. 14. Investigation of the moment of drop detachment, satellite drop formation and its movement.

2.3 Secondary Breakup with Airblast atomization

When the liquid jet is injected into the coflowing high speed airflow, the liquid jet breaks up owing to momentum transfer from the gas to the liquid. This type of breakup is often referred to as air-blast atomization.

2.3.1 Shear thickening droplet

Experimental Setup : Different solutions of cornstarch-water, Coal Water slurry, and Syrup-water are prepared.

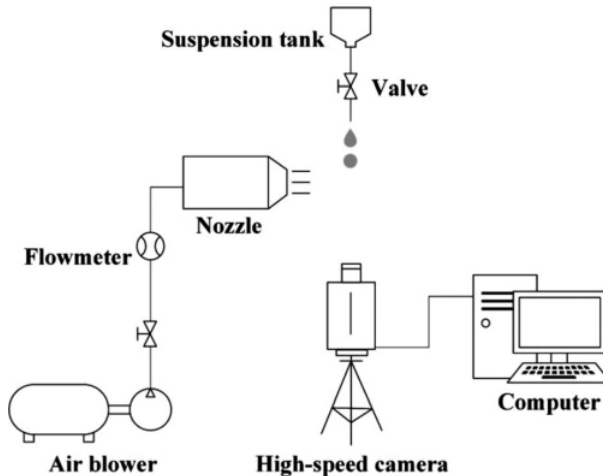


FIG. 2. Schematic of the secondary atomization experimental apparatus.

Results and Discussions

The apparent viscosity μ of the suspension of ϕ 49% fluctuates slightly when the shear rate $\dot{\gamma}$ is relatively low; this property is similar to those of Newtonian fluids.

The complete analysis of the rheological properties of the testing fluids can be understood by the following diagram.

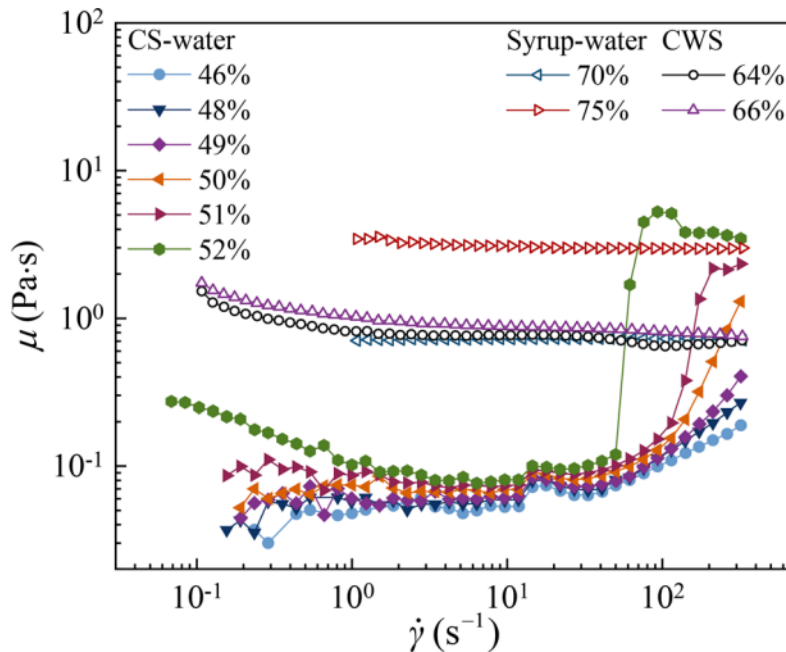


FIG. 3. Rheological property measurements.

Droplets in the cornstarch-water suspension with a viscosity ratio (u) below 48% display a secondary breakup morphology akin to that observed in Newtonian fluids, as depicted in Figures 4-6. For viscosity ratios below 48%, various breakup modes such as Multimode (Stamen, Hole), Bag, and Shear are observed.

The secondary breakup phenomenon in Newtonian fluids is attributed to the interplay between aerodynamic forces and surface tension. Surface tension serves to maintain droplet integrity or allows for deformation without breakup when aerodynamic forces are relatively subdued.

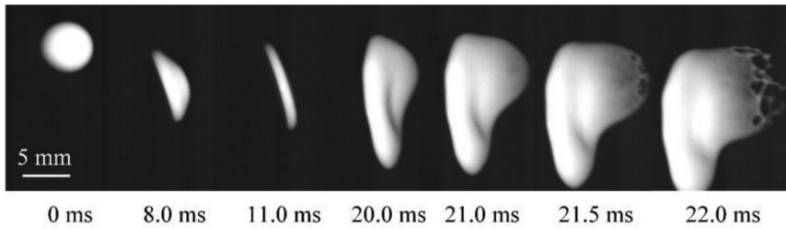


FIG. 4. Bag breakup of the cornstarch–water suspension; the air flows from left to right ($\varphi = 46\%$, $u_g = 15.3 \text{ m/s}$).

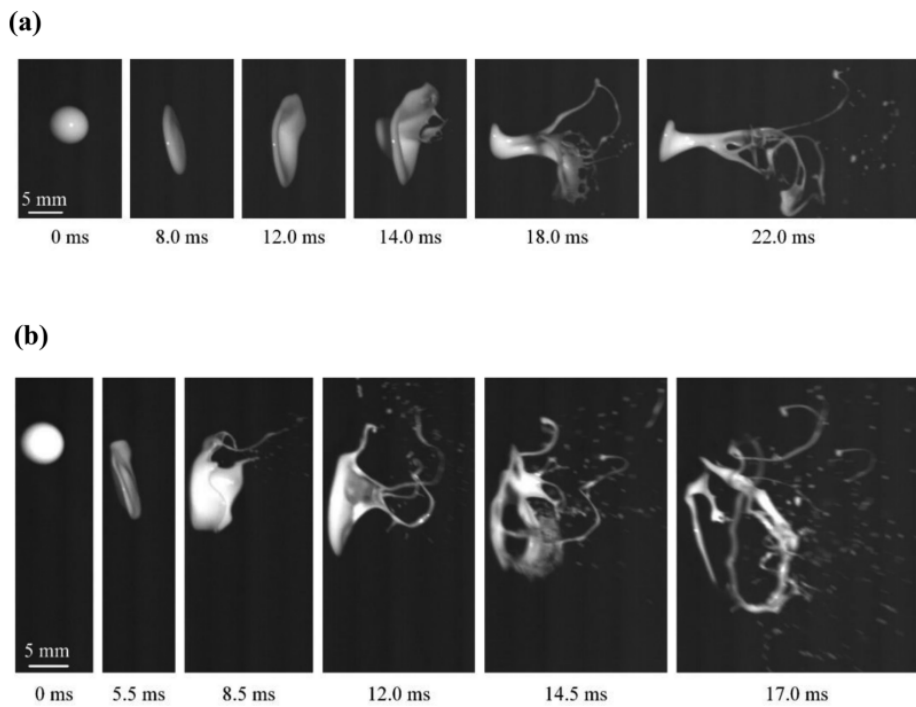


FIG. 5. Multimode breakup of the cornstarch–water suspension; the air flows from left to right. (a) Stamen structure $\varphi = 46\%$, $u_g = 23.0 \text{ m/s}$ and (b) hole structure $\varphi = 46\%$, $u_g = 30.6 \text{ m/s}$.

At a suspension concentration where $\phi = 49\%$, the system displays transitional behavior. Specifically, under low air speeds, the suspension undergoes a bag-like breakup pattern. However, as air speed increases, neither multimode nor shear breakup modes manifest.

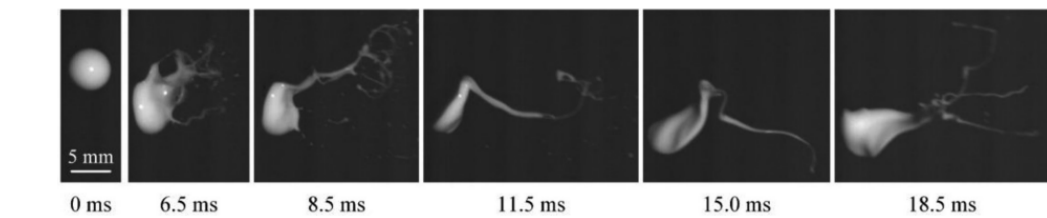


FIG. 7. Fiber breakup of the cornstarch–water suspension; the air flows from left to right ($\varphi = 49\%$, $u_g = 38.3 \text{ m/s}$).

Suspension droplets with a viscosity ratio exceeding 49% demonstrate hardened deformation as air speed escalates into the high range. The high shear rate caused by high speed air results in the DST(Discontinuous Shear Thickening) rheological behavior of suspension. The windward side of the droplet deforms into a sheet, while the leeward side remains hemispherical, and the droplet maintains this hemispherical shape until it leaves the airflow field.

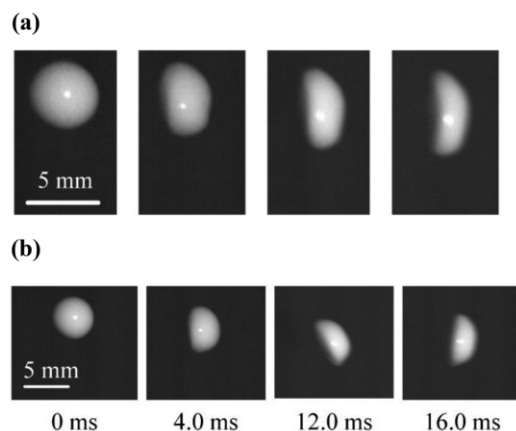


FIG. 8. Hardened deformation of the cornstarch–water suspension; the air flows from left to right. $\varphi = 51\%$, (a) $u_g = 61.2$ and (b) $u_g = 76.5 \text{ m/s}$. Multimedia view: <https://doi.org/10.1063/5.0062345.1>

Dimensionless Number : N

A dimensionless number N is formulated which is used to compare relative magnitude of the increments of viscous and the aerodynamic force.

$$N = \frac{\frac{d}{du_g} K \dot{\gamma}^n}{\frac{d}{du_g} \rho_g u_g^2} = \frac{K n u_g^{n-1} D_0^{-n}}{2 \rho_g u_g} = \frac{Kn}{2 \rho_g} u_g^{n-2} D_0^{-n}.$$

The below figure depicts the dimensionless number N for various breakup conditions.

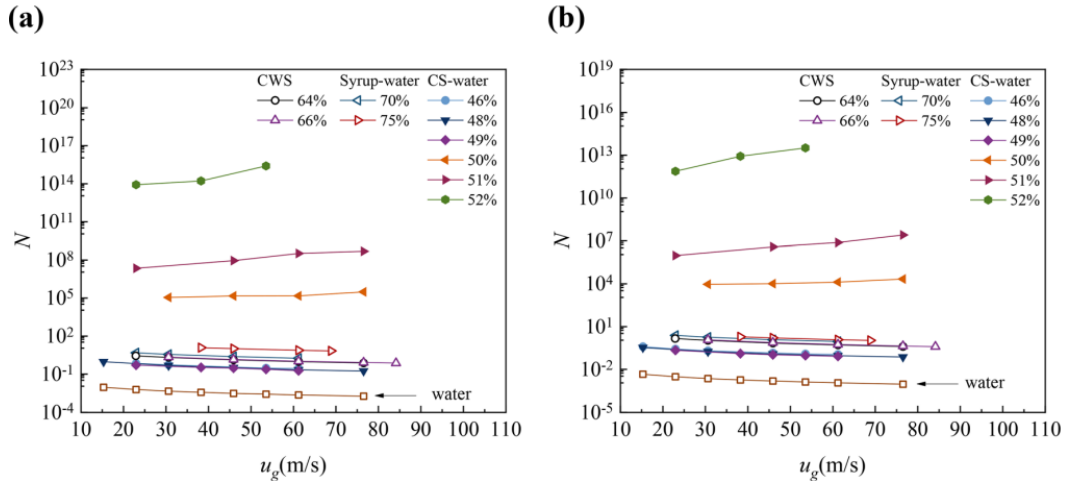


FIG. 11. Dimensionless number N in secondary breakup; here, the initial diameters of droplet D_0 are (a) 2.5 and (b) 5.0 mm.

Breakup Regime Map :

Based on the data, we can formulate a decision line for the conditions of hardened deformation and Newtonian fluid secondary breakup. The decision boundary line is around $N \approx 10$

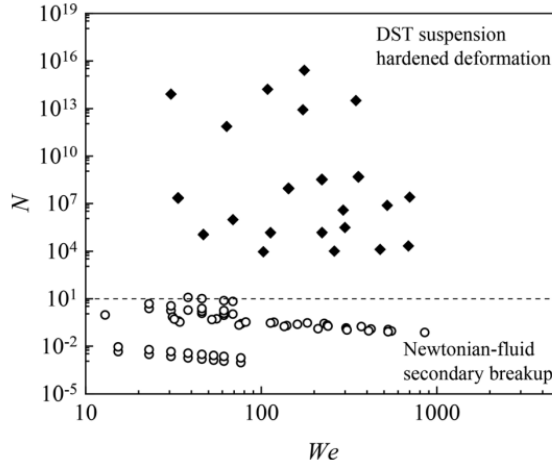


FIG. 12. Deformation and breakup regime map, where hollow and solid illustrations represent different modes.

Morphological properties of droplets

D_{max}/D_0 is used to represent the deformation degree of suspension droplets. D_0 is the initial diameter of the droplet, and D_{max} is the maximum diameter of the oblate sheet into which the droplet deforms.

The volume of the suspension droplet during the deformation is constant, which is represented as $V_0 = V_{max}$.

$$\frac{4}{3}\pi\left(\frac{D_0}{2}\right)^3 = \frac{2}{3}\pi\left(\frac{D_{\max}}{2}\right)^3.$$

The D_{\max}/D_0 is

$$\frac{D_{\max}}{D_0} = \sqrt[3]{2} \approx 1.26.$$

Experimentally found out,

$$D_{\max}/D_0 = \begin{cases} 1.76, & N \leq 10, \\ 1.18, & N > 10. \end{cases}$$

2.3.2 Shear thinning droplet

This experiment uses a solution of coal-water slurry which is a shear thinning suspension. Coal water slurry (CWS) is a fuel which consists of coal particles suspended in water, which is widely used in coal combustion and gasification.

Experimental setup and methodology

Coal particle size cumulative distributions are given in Figure. In this test the coal type is bituminous coal, whose density is 1490 kg/m^3 . The basic shapes of the particles are shown in Fig.

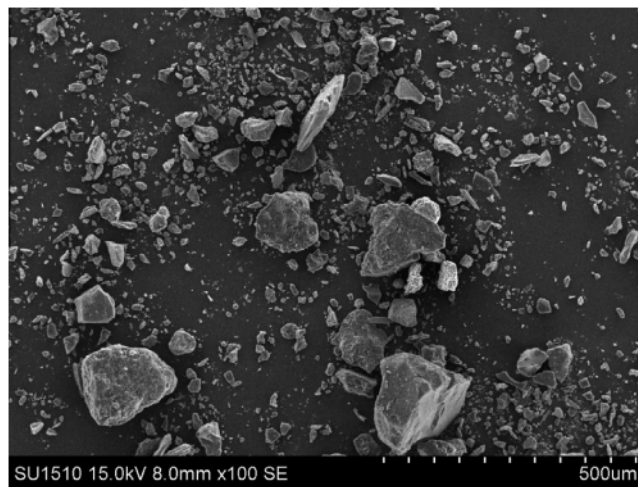


Fig. 1b. SEM of coal particles.

Three types of Cornstarch-Water Suspensions (CWS) were examined, labeled as A ($\phi = 0.555$), B ($\phi = 0.566$), and C ($\phi = 0.575$), each with varying concentrations, ϕ being the volume fraction. Initially, viscosity demonstrates a decreasing trend, followed by fluctuations across different concentrations. Notably, viscosity exhibits an increasing trend with the volume fraction of solute.

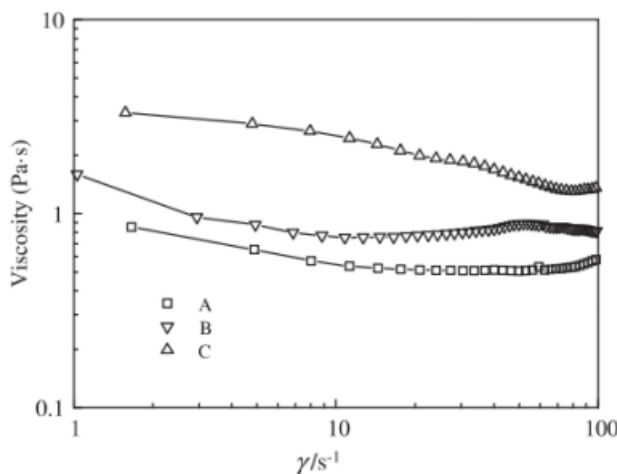


Fig. 2a. Viscosity of CWS against the shear rate.

To quantify the viscoelastic properties, N1, defined as the difference between τ_1 (stress along the flow direction) and τ_2 (stress perpendicular to the flow direction), was utilized. N1 serves as a measure of viscoelasticity within the system.

Frequency of Primary Atomization

The shear wave is from the development of Kelvin–Helmholtz instability. It is observed at high liquid velocity. However, the viscoelasticity would hinder the development of instability wave on liquid surface. When the viscoelasticity is high the structures of shear wave become indistinct, which results in the disappearance of many ligaments. Oscillating jet is observed at low velocity only. The Strouhal number (St) is the dimensionless number which is useful for analyzing oscillating unsteady fluid flow dynamics problems. St is given by fD_1/u_l

Strouhal number can be found out by two frequencies - Shear frequency and Oscillation frequency.

Breakup morphology of secondary atomization

In secondary atomization processes, the aerodynamic force acts as a disruptive influence, while the surface tension, viscous force, and elastic force serve stabilizing functions.

Multimode breakup occurs when the aerodynamic force approaches equilibrium with the stabilizing forces. This phenomenon encompasses various breakup modes, including hole and tensile breakup types. Specifically, when both the yield and elastic forces are relatively small, as observed in Newtonian Fluid CWS A, multimode breakup predominates. Conversely, in cases where both the yield stresses are significant, such as in CWS B and C, the breakup mechanism shifts towards tensile breakup, resulting in a highly

intricate breakup pattern.

In the context of secondary atomization, time is commonly expressed in nondimensional form,

$$T = \frac{u_g t}{D_0 (\rho_l / \rho_g)^{1/2}},$$

where 't' represents the dimensional time elapsed from the initial spherical drop to the formation of an oblate spheroid.

Temporal properties of drop formation When the minimum neck diameter significantly exceeds the size of the coal particle, the Cornstarch-Water Suspension (CWS) demonstrates effective fluid-like behavior. Under these conditions, the evolution of the minimum neck diameter over time follows a power law relationship characterized by a 2/3 power law.

However, as the minimum neck diameter approaches the size of the coal particle, the homogeneity of the CWS is compromised. In this scenario, the suspension can no longer be accurately characterized as a homogeneous fluid.

The best fit time correlation :

$$T = 1.9(We_s - 12)^{-0.25}(1 + 4.5Oh_s^{0.45})(1 + 8.5 \times 10^{-3}X_s^{0.011}).$$

Conclusions In primary atomization, the length of breakup plays a crucial role in determining atomization efficiency. A dimensionless correlation for Coal Water slurry (CWS) jet breakup length has been derived using a KH-RT hybrid model. The findings indicate that the ratio of breakup length to initial droplet diameter (L_b/D_0) decreases with increasing Momentum flux mass ratio(M) and Weber number in primary atomization (We_p), while it increases with increasing Ohnesorge number in primary atomization (Oh_p) and ratio of first normal stress difference to surface tension force in primary atomization (X_p).

Two distinct periodic structures are observed in CWS primary atomization: shear wave and jet oscillation. Shear structures are predominant under conditions of high liquid velocity and low liquid viscoelasticity, whereas oscillation structures prevail under conditions of low liquid velocity and high liquid viscoelasticity.

In secondary atomization, various breakup modes are identified, including no breakup,

hole breakup, tensile breakup, and shear breakup. The viscoelastic properties of the liquid exert significant influence on the breakup morphology of CWS droplets.

Moreover, the deformation scale of secondary atomization decreases with increasing liquid viscoelasticity, while the deformation time of secondary atomization increases with increasing liquid viscoelasticity.

2.4 Drop Impact

Drop impact experiments were conducted utilizing micro-patterned surfaces to investigate the interaction of non-Newtonian liquids under controlled conditions. Two types of non-Newtonian liquids were studied: shear-thickening liquids, exemplified by cornstarch at a concentration of 30%w/w, and shear-thinning liquids, represented by Carbopol. The impact behavior of these liquids was analyzed concerning surface properties and microstructure, with particular attention to deviations from traditional scaling laws observed in previous studies.

Formation of Carbopol Solution

De-ionized water was slowly added at 50under constant mixing for two hours. At this point, the Carbopol solution was purchased and is highly acid ($\text{pH} = 3$), and sodium hydroxide solution at 18added to bring the pH up to 7. After stirring at 700 rpm to remove air bubbles and lumps, a transparent gel is obtained. Two different concentrations of Carbopol were used, 0.2% and 1%w/w.

Cornstarch at a concentration of 30%w/w, conforms to the scaling laws of Newtonian fluids at relatively low concentrations. Additionally, visco-elastic liquids, exemplified by Carbopol, are studied in terms of their impact behavior on both hydrophilic and superhydrophobic surfaces. Our observations reveal deviations in scaling laws when these liquids interact with superhydrophobic surfaces, contrary to predictions based on hydrophilic surfaces.

For inviscid liquids, one may expect the kinetical energy to be totally transmitted into the spreading, which will have an energetic cost proportional to the liquid surface tension γ .

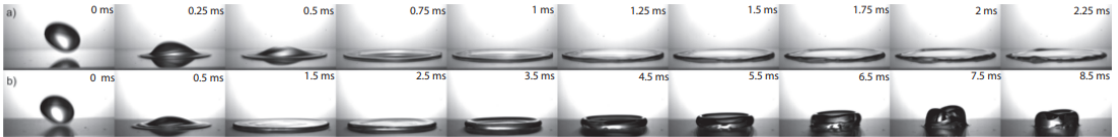


FIG. 3. Side-view sequence of snapshots of Carbopol 1%tw drops of 4mm in diameter at 5 m/s ($We \sim 1000$) (a) on smooth glass and (b) on a superhydrophobic surface. Note the lack of splash in both cases in spite of the high Weber number, and the fast recoil of the droplet on the superhydrophobic surface.

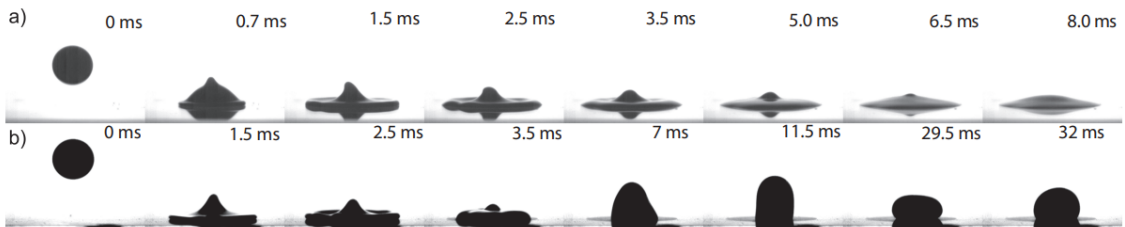


FIG. 7. Side-view sequence of snapshots of cornstarch suspension drop of 2.5mm at $U \approx 4.6 \text{ m/s}$ on (a) smooth glass and (b) superhydrophobic surface (total time 25ms). Note that the impact on the superhydrophobic surface (b) does produce a significant splash as well as a strong recoil.

The maximum diameter attained by the liquid film, denoted as D_{max} , and the initial drop size, represented as D_0 , were investigated. Our analysis suggests that there is minimal disparity in drop impact behavior between glass and PDMS surfaces. Notably, significant deviations in behavior were observed only at Weber number (We) approximately equal to 1000.

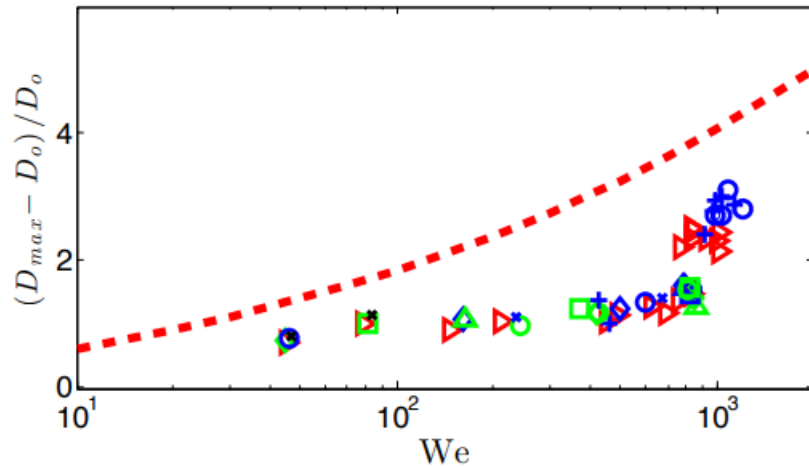


FIG. 2. The spread factor $(D_{max} - D_0)/D_0$ plotted as a function of Weber number for Carbopol 1% drops. The scaling law found for water on superhydrophobic surfaces⁵: $D_{max}/D_0 = 0.9We^{1/4}$ is plotted as a dashed thick line as a reference.

On a partially wetting surface, visco-elastic droplets exhibit a spreading behavior that appears independent of droplet size, at least within a certain range, typically spanning a decade. In the given experiment, drop size was 8 mm to 27 mm.

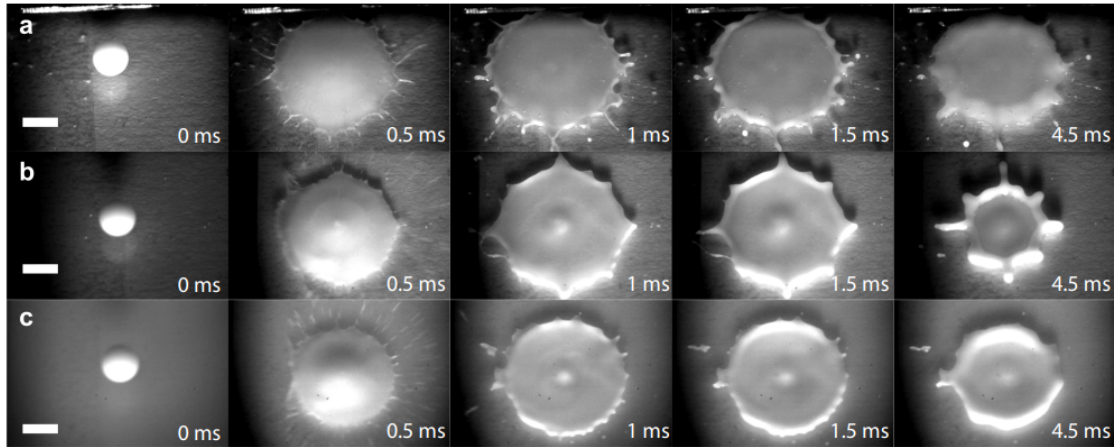


FIG. 8. Top view sequence of cornstarch drops impacting onto hydrophobic, square-lattice microstructures with three periodicities: (a) $d = 8\mu\text{m}$, (b) $d = 15\mu\text{m}$, (c) $d = 25\mu\text{m}$. The bars indicate a length scale of 2mm.

As can be seen in figures 8a and 8b, when the drop impacts on a distinct regular pattern, the splashing is driven in specific directions, which are strongly correlated with the lattice arrangement. Hexagonal and square-lattice arrays of micropillars were used to explore the role of the geometrical distribution of micro-pillars of cylindrical micron-sized 3 pillars of width w , height h , and interspace d .

Directional splashing is originated by air flow generated beneath the drop which is squeezed out. Air flow might reach large enough velocities to drag some liquid with it and promote fingering and splashing, in the direction permitted by lattice arrangement. When d is big enough, splashing becomes more complex air flow velocity gets very high. The cornstarch drops show a more pronounced directional recoiling than spreading/splashing, which could be qualitatively understood in terms of the shear-thickening character of cornstarch.

Besides this complex behavior and in spite of the expected local increase of viscosity, the 30%w cornstarch drops seem to spread following the same scaling with the Weber number as a Newtonian fluid. Non-newtonian behavior of cornstarch is not activated at this concentration.

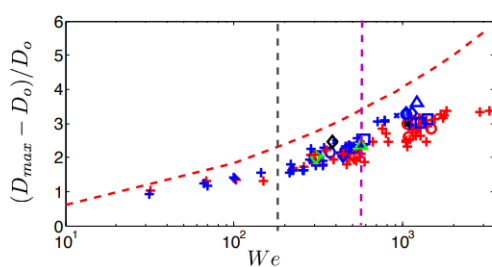


FIG. 9. The spreading factor $(D_{max} - D_o)/D_o$ for impacting cornstarch droplets plotted as a function of Weber number. The scaling law found for water on superhydrophobic surfaces⁵ is plotted as a dashed thick line as a reference. The vertical lines correspond to the splashing limits on PDMS (left) and on glass (right).

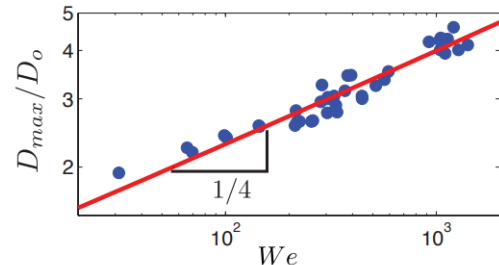


FIG. 10. D_{max}/D_o for impacting cornstarch droplets plotted as a function of Weber number in logarithmic scale. The continuous thick line with slope 1/4 shows that cornstarch 30% clearly follows the same exponent as that found for Newtonian liquids for Weber numbers up to 2000.

2.5 Shear and Extensional Flow

Introduction

Dense suspensions of model hard-sphere (HS)-like colloids, with different particle sizes, are examined experimentally near and in the glass state, under shear and extensional rheology. Under steady shear flow, we detect both continuous and discontinuous shear thickening (DST) above a critical shear rate (or shear stress), depending on the particle size and volume fraction. Start-up shear experiments show stress overshoots in the vicinity of the onset of DST indicative of microscopic structural changes, while the sample macroscopically shows dilatancy effects.

Samples and Setup

Colloidal glasses samples consist of nearly hard-sphere (HS) particles with varied sizes and polydispersity. Particles are composed of polymethyl methacrylate (PMMA) and are sterically stabilized by a thin grafted layer of poly-12-hydroxystearic acid (PHSA) chains. PHSA induces steric repulsion, stabilizing particles against van der Waals attractions, creating an almost ideal HS interaction. PMMA particles are dispersed in squalene, a nonvolatile solvent with properties similar to PMMA, minimizing residual van der Waals attractions.

A cone and plate geometry attached to an Anton Paar MCR 501 rheometer was used for the shear experiments.

The extension measurement was done using the capillary breakup extensional rheometer (Haake CaBER-1) and the filament stretching rheometer (FSR) (VADER 1000 by Rheofilament)

Shear measurements

The first normal stress difference $N_1 = \sigma_{xx} - \sigma_{yy}$, where σ_{xx} is the stress acting normal to the shear plane and σ_{yy} is the stress acting normal to the shear gradient plane, extracted from the axial force measured by the transducer, $2F_y = N_1\pi r^2$ Brownian time is defined by :

The shear rate is multiplied by the Brownian time, to get a non dimensional shear rate: $Pe = \dot{\gamma} t_B = \dot{\gamma} 6 \pi \eta_R^3 / k_B T$

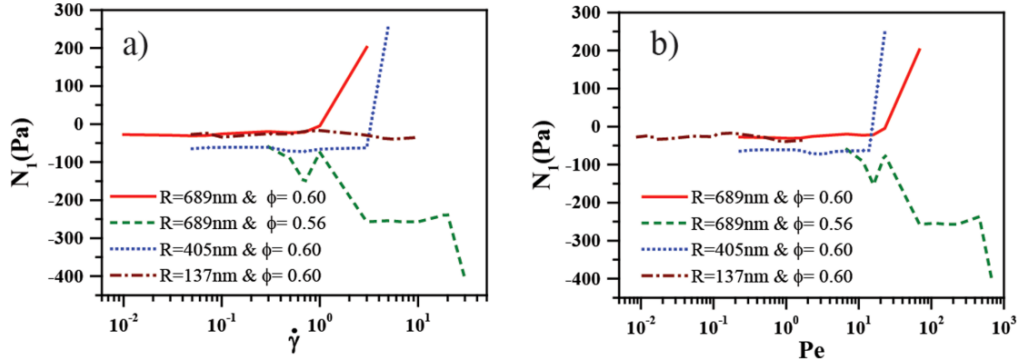


FIG. 4. (a) First normal stress difference, N_1 , as a function of shear rate for all samples measured as indicated. (b) The same data as in (a) plotted versus the dimensionless shear rate, Pe .

At the highest shear rates measured however, for both particles shown in Fig. 6, we detect first an increase in σ_N to positive values in the vicinity of the first stress overshoot and subsequently a drop to negative values around strains where the second stress overshoot is detected, as seen at lower shear rates. This is due to dilatancy accompanied stick slip behavior and flow instabilities.

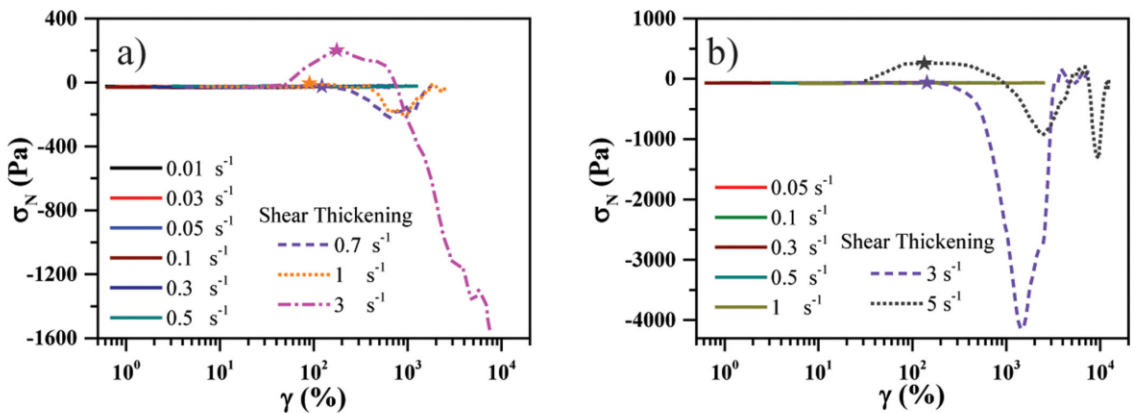


FIG. 6. Normal stress $\sigma_N = 2F_y/\pi r^2$ during transient start-up shear experiment versus strain, γ , for particles with $R \approx 689$ nm (a) and $R \approx 405$ nm (b). All samples were measured at a volume fraction of $\phi \approx 0.60$. The asterisks denote the point in time (or strain), where the effective viscosity data plotted in Fig. 4 were determined.

The experiments were performed in a cone-plate geometry, rather than in a plate-plate with a varying gap. Along these lines, we also performed measurements with a cone-partition-plate (CPP) geometry. The onset of shear thickening both in steady shear measurements as well as in oscillatory shear was not affected by the use of the CPP. Although some details of the curves are different, no significant changes were detected with the use of the CPP.

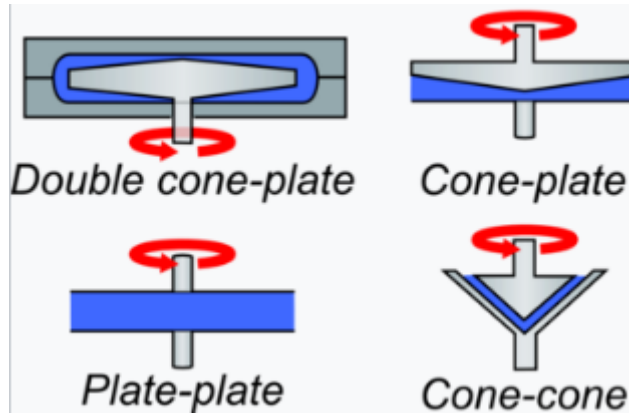


Figure 2.8: Rotational geometries of different types of shearing rheometers

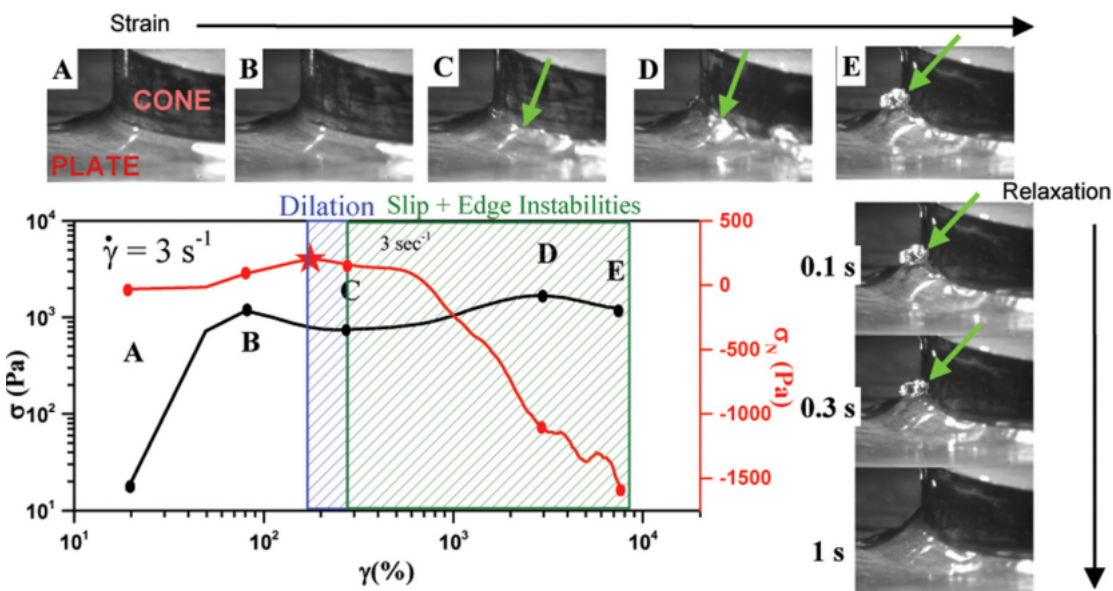


Figure 2.9: Rotational geometries of different types of shearing rheometers and stages of step-rate experiments monitored by video recorded images following the stress and normal stress as a function of strain for: (a) System with large particles, $R = 689 \text{ nm}$ at constant shear rate, $\dot{\gamma} = 3 \text{ s}^{-1}$. Stars indicate the position in time where the values of the shear and normal stress were determined, prior to the dilatancy.

CABER Extension

For all samples, similar to shear measurements, there is a critical value of the strain rate, $\dot{\varepsilon}_c$, determined by visual observation.

At higher rates, $\dot{\varepsilon}_0 > \dot{\varepsilon}_c$, the samples with the two larger particles exhibit a brittle solidlike response manifested by a break-up with an irregular shape during the stretching period.

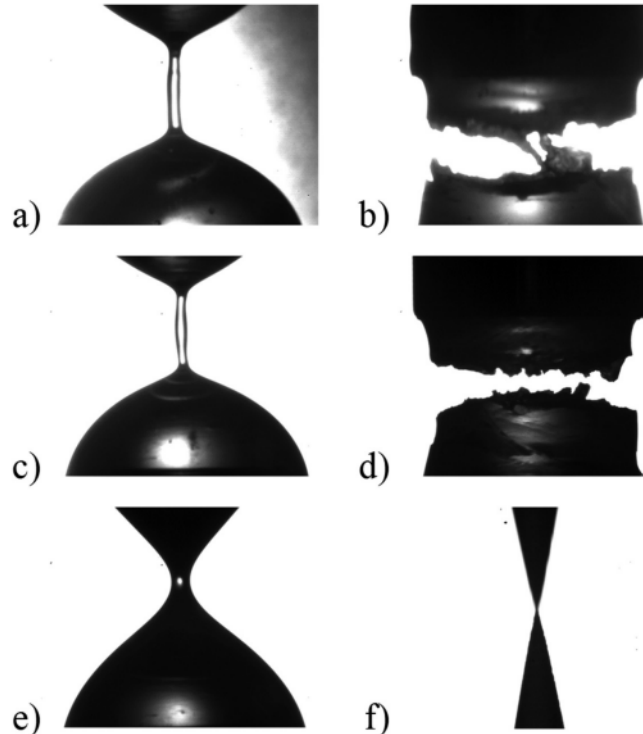


FIG. 8. Final filament shape for HS glasses with particle size $R \approx 689$ nm (top), $R \approx 405$ nm (middle) and $R \approx 137$ nm (bottom) for low ($\dot{\varepsilon}_0 < \dot{\varepsilon}_c$, left) and high ($\dot{\varepsilon}_0 > \dot{\varepsilon}_c$, right) extension rates. All samples are at $\varphi \approx 0.60$. These characteristic filament shapes were obtained with the CaBER set-up.

U. Freudenthal et al.

The breakup behaviour is seen in almost all cases except the lowest shear rate.

For $\dot{\varepsilon}_0 > \dot{\varepsilon}_c$, samples with the two larger particles ($R \approx 405$ nm and $R \approx 689$ nm) exhibit a brittle failure reminiscent of crystalline solid materials. Under these conditions, the samples fracture without any apparent yielding and plastic deformation observed [Figs. 8(b) and 8(d)]. Experiments with the smallest particles ($R \approx 137$ nm), however, reveal a highly ductile behavior under elongation, with the sample flowing until it necks, due to plastic deformation allowed in the microstructure.

FSR Extension

For the smaller particle samples ($R \approx 137$ nm), a liquid-like behavior was always seen in the range of the equipment (maximum strain rate of 20 s^{-1}). For samples with

particle sizes $R \approx 405$ nm and $R \approx 689$ nm, we find again a critical strain rate, ε_c above which the filament structure changes and the sample shows a solid like response with an irregular shape and rough texture. The strain rate measured in the FSR is deduced using the filament mid-point diameter, while the strain rate in the CaBER is estimated from the velocity of the moving plates. The critical shear rate measured through CaBER are lower than the FSR measurement.

Chapter 3

Conclusion

Contents

3.1 Further Applications	30
3.1.1 Liquid Armor	30

3.1 Further Applications

Typical shear thickening fluids such as polyoxyethylene, polyacrylamide, olefin homopolymer, and polymethacrylate can be used as drag reducing agents in water or other solvents. The reduction of drag leads to increased pipeline capacities and decreased resistance on the ships. Furthermore, the addition of polyoxyethylene to firefighting foams reduces the fluid flow resistance and leads to higher fire water head.

Non-Newtonian fluids are also utilized to improve the quality of printing technologies. Studies show that thixotropic or shear thinning fluids such as sodium alginate, modified starch, and cellulose derivatives can be utilized as natural thickeners in the printer ink. These non-Newtonian fluids improve the viscosity and the flow behavior of the ink providing a clearer printing experience.

Non-Newtonian fluids are also utilized in damper and brake systems. The modified dimethyl silicone oil is used as the magnetorheological fluid in dampers and brakes. The viscosity of non-Newtonian fluids used in these systems increases in the magnetic field and improves energy dissipation. Dampers are used in noise reduction systems of washing machines, building seismicity, and carrier-based aircraft interception systems. Brakes are utilized for the control of the rotational speed of motors.

3.1.1 Liquid Armor

Introduction

It is important to separate stab threats into two specific mechanisms: puncture and cut. Puncture refers to impact by instruments such as ice picks or awls, which have a

sharp tip but no cutting edge. Cut refers to impact by knives with a continuous cutting edge. Knife threats are generally more difficult to stop than puncture.

A number of commercial stab-protective materials are available. There are a number of problems with the usage of the existing materials, namely, heavy weight, expensive, and not appropriate protection. More recent material research efforts include thermal-sprayed hard ceramic coatings onto woven aramid fabrics.

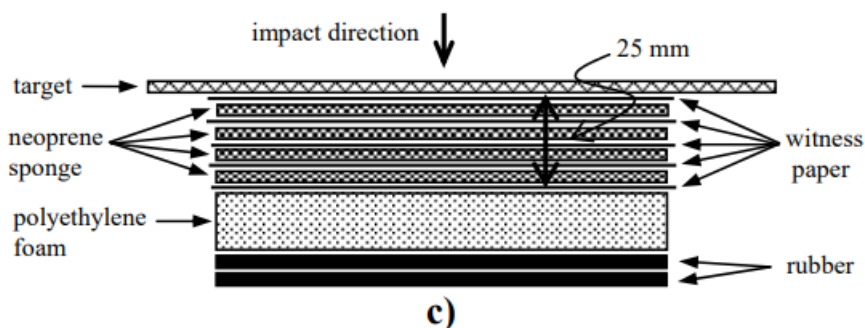
These hard-coated fabrics demonstrate increases in energy absorption during quasi-static stab tests, as compared with uncoated fabrics. However, these coatings also add significant weight to the fabric.

Investigation was done into the ballistic properties of woven aramid fabrics treated with a colloidal, discontinuous shear thickening fluid (STF). A discontinuous STF undergoes a significant increase in viscosity with shear rate, transitioning from a flowable liquid to a solid-like state when deformed quickly. Our findings revealed that under certain conditions, this STF-fabric composite exhibits ballistic properties superior to those of neat fabrics. Furthermore, the addition of STF resulted in minimal to no increase in the thickness or stiffness of the fabric.

Material

Targets were made from plain-woven Hexcel-Schwebel Style 706 fabric composed of Kevlar KM-2 fibers. Shear thickening fluids (STF) were created by dispersing colloidal silica particles in polyethylene glycol, with ethanol added as a co-solvent to adjust viscosity and surface tension. Twelve layers of Kevlar fabric were impregnated with the ethanol/STF mixture and heated to remove ethanol. The resulting STF concentration in the fabric was approximately 20% by weight. A 12-layer STF-Kevlar target and a comparison target consisting of neat Kevlar fabric were fabricated for experimental analysis.

Drop tower stab testing



c) Multi-layer foam backing construction.

Stab tests involve mounting the impactor to a crosshead loaded with specific masses. The crosshead is dropped from a fixed height to strike the target. Velocity at impact is measured using fixed flags and sensors. Impact loads are measured using a load cell mounted to the impactor. Depth of penetration into the target is quantified by the number of witness paper layers penetrated. There are five layers of witness paper, with the maximum reported penetration depth being five layers. For the experiment, either the mass was fixed and height was varied or height was fixed and mass was varied. This approach is different from that of NIJ - National Institute of Justice so the values can't be directly compared with them. Experiments were done for both neat Kevlar and STF Kevlar.

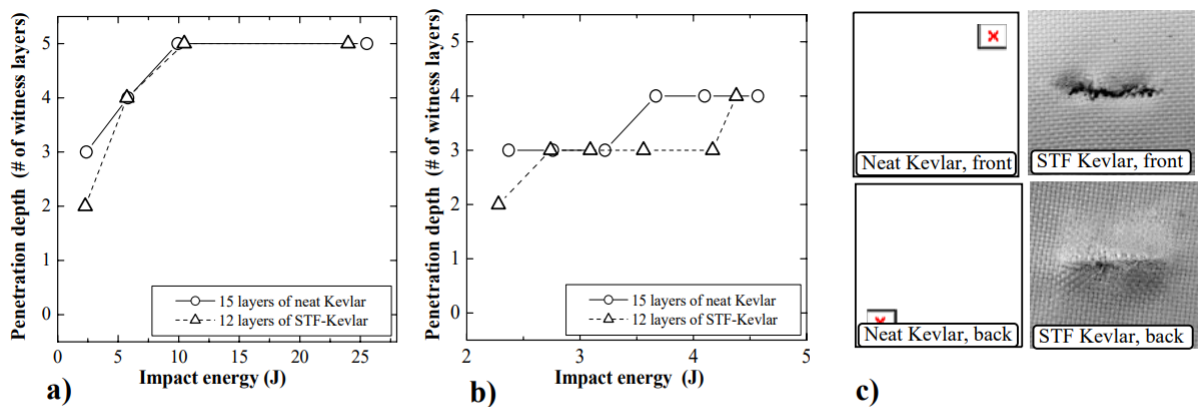


Figure 2. a) Knife impactor penetration depth vs. impact energy performed at fixed crosshead mass and several impact velocities. b) Knife impactor penetration depth vs. impact energy performed at fixed impact velocity and several crosshead masses. c) Photographs of targets following knife impact (velocity = 4.6 m/s, mass = 2340 g, energy ~ 25 J)

Quasistatic testing

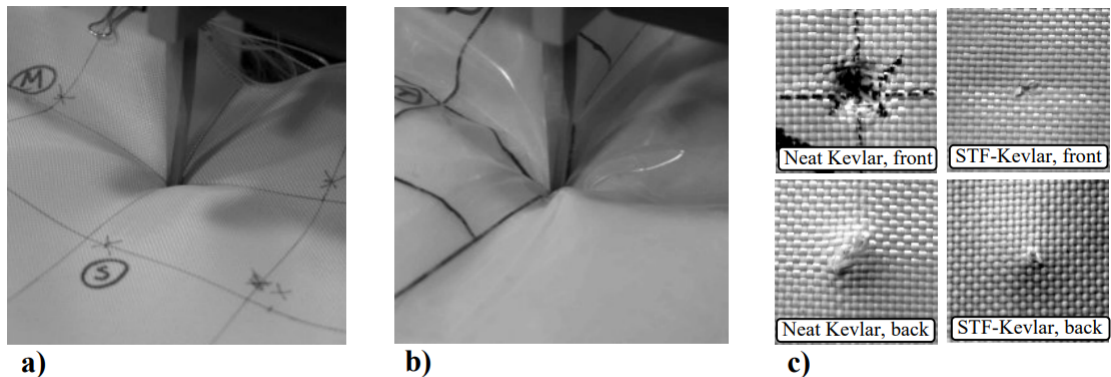


Figure 4. a) Quasistatic testing of neat Kevlar target using knife impactor. b) Quasistatic testing of STF-Kevlar using knife impactor. c) Photographs of target materials after testing.

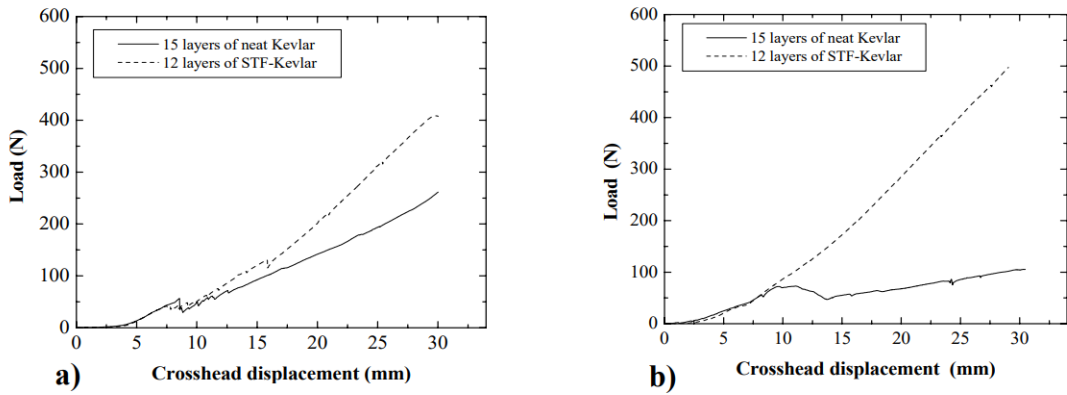


Figure 5. a) Load versus displacement during quasistatic knife testing. b) Load versus displacement during quasistatic spike testing.

Conclusions

Stab test results indicate that STF-Kevlar is slightly more efficient against knife threats compared to neat Kevlar, per-mass basis. STF-Kevlar exhibits dramatically improved effectiveness against spike threats compared to neat Kevlar, per-weight and per-layer basis. STF likely enhances yarn mobility, preventing yarn sliding and separation, thus improving engagement with the spike. STF-Kevlar demonstrates superior stab protection, particularly in puncture resistance, compared to neat Kevlar fabric. STF-fabric composites offer advantages including simple production processes, applicability to various high-performance fabrics, cost-effectiveness, thinness, flexibility, and potential for enhanced ballistic properties. This material has the potential to provide multi-threat protection (both ballistic and stab) in a single material.

Chapter 4

References

All the images used in the above report are snipped from the following list of research papers.

- [1] Wang, Zi-Yu, Hui Zhao, Wei-Feng Li, Jian-Liang Xu, and Hai-Feng Liu. "Breakup of shear-thickening suspension." *Phys. Rev. Fluids* 7, no. 7 (2022): 073601. DOI: 10.1103/PhysRevFluids.7.073601
- [2] Ricardo J. E. Andrade, Alan R. Jacob, Francisco J. Galindo-Rosales, Laura Campo-Deaño, Qian Huang, Ole Hassager, George Petekidis; Dilatancy in dense suspensions of model hard-sphere-like colloids under shear and extensional flow. *J. Rheol.* 1 September 2020; 64 (5): 1179–1196. <https://doi.org/10.1122/1.5143653>
- [3] Guémas, Marine, Álvaro G. Marín, and Detlef Lohse. "Drop impact experiments of non-Newtonian liquids on micro-structured surfaces." *Soft Matter* 8, no. 41 (2012): 10725-10731. DOI: 10.1039/C2SM26230D
- [4] Zhao, Hui, Yan-Bing Hou, Hai-Feng Liu, Xiu-Shan Tian, Jian-Liang Xu, Wei-Feng Li, Yi Liu, Fu-Yu Wu, Jie Zhang, and Kuang-Fei Lin. "Influence of rheological properties on air-blast atomization of coal water slurry." *Journal of Non-Newtonian Fluid Mechanics* 211 (2014): 1-15. DOI: 10.1016/j.jnnfm.2014.06.007
- [5] Salehi, Moloud Sadat, Mohamad Taghi Esfidani, Hossein Afshin, and Bahar Firoozabadi. "Experimental investigation and comparison of Newtonian and non-Newtonian shear-thinning drop formation." *Experimental Thermal and Fluid Science* 94 (2018): 148-158. DOI: 10.1016/j.expthermflusci.2018.02.006
- [6] Ron Egres, Yuan-Shin Lee, J. Kirkwood, Keith Kirkwood, E. Wetzel, and Norman Wagner. "Liquid armor: Protective fabrics utilizing shear thickening fluids."
- [7] Zi-Yu Wang, Hui Zhao, Wei-Feng Li, Jian-Liang Xu, and Hai-Feng Liu. "Secondary breakup of shear thickening suspension drop." *Physics of Fluids* 33, no. 9 (2021): 093103. DOI: 10.1063/5.0062345

- [8] Jianbin Qin, Borui Guo, Le Zhang, Tianwei Wang, Guangcheng Zhang, and Xuetao Shi. "Soft armor materials constructed with Kevlar fabric and a novel shear thickening fluid." Composites Part B: Engineering 183 (2020): 107686. DOI: 10.1016/j.compositesb.2019.107686